Smart Mater. Struct. **18** (2009) 125002 (7pp) doi:10.1088/0964-1726/18/12/125002

A novel multi-axis force sensor for microrobotics applications

R J Wood[1], **K-J Cho**[2] **and K Hoffman**[1]

[1] School of Engineering and Applied Sciences, Harvard University, USA
[2] School of Mechanical and Aerospace Engineering/IAMD, Seoul National University, Korea

E-mail: rjwood@seas.harvard.edu, kjcho@snu.ac.kr and khoffman@seas.harvard.edu

Received 12 March 2009, in final form 22 July 2009
Published 23 September 2009
Online at stacks.iop.org/SMS/18/125002

Abstract
High performance force sensors often encounter the conflicting requirements of fine sensitivity and wide bandwidth. While there is an intrinsic tradeoff between these two metrics that cannot be physically avoided for any force transducer, through proper optimization the product of these two can be maximized. Similarly, the requirements of multiple sensing axes and overall compactness are also often at odds. This paper describes a novel design, simple method of fabrication, and thorough analysis of a high performance two-axis force sensor. We conclude with an example application: measuring the lift and drag forces from a flapping-wing robotic insect.

(Some figures in this article are in colour only in the electronic version)

1. Introduction

There are myriad applications which require force sensors with fine sensitivity and a large bandwidth [1–4]. These two requirements are conflicting: all solid-state force transducers operate by converting an applied stress (force) into a material strain (deformation). This strain is then sensed optically, capacitively, piezoelectrically [5], or piezoresistively [6–8] and converted to force information by a calibration procedure. The geometry and physical properties of the transducer then fully define the static and dynamic response, and therefore the sensitivity and the bandwidth. Take the case of a simple clamped-free cantilever beam: a force applied to the distal end of the beam results in a displacement that can be measured and converted to force by a pre-determined calibration. The stiffness of the beam determines the force–displacement relationship. To achieve greater sensitivity, the beam could be made more compliant, resulting in greater deformations for a given load. To increase the bandwidth, the beam could be made more stiff, increasing the natural frequency of the beam[3]. Hence the paradox.

Traditional force sensors typically optimize sensitivity at the expense of resonant frequency (e.g. precision scales), or maximize resonant frequency at the expense of sensitivity (e.g. strain-gauge load cells [9]). Various types of silicon micro-machined sensors with high sensitivity have been developed for biomedical applications, measurement and handling of microcomponents, etc. Piezoresistive force sensors has been developed for atomic force microscopy [10]. Sun *et al* developed a microforce sensor with a comb drive configuration to characterize a flight of a fruit fly [11]. Beyeler *et al* developed a microforce/torque sensor using capacitive comb drive for magnetic microrobots [12]. Tibrewala *et al* developed a miniaturized bulk micro-machined three-axes piezoresistive force sensor [13]. Some of these silicon micro-machined sensors are even commercially available (e.g. FemtoTools). Micro-machined sensors are small, light-weight and have high sensitivity and high resonant frequencies. But their resonant frequency drops significantly once a mass that is comparable to its equivalent mass is fixed to the input. For meso-scale microrobots, e.g. the Harvard Microrobotic Fly [14], the mass ranges from 10 to 150 mg, typically well outside the sensing range for these sensors. Furthermore, even if it were possible to fix these microrobots to such sensors, the resonant frequency, and hence the bandwidth, of the sensor would drop below the required resonant frequency.

Adding more sensing degrees of freedom further complicates the design [8, 15]. This paper describes a new two-axis force sensor that is optimized to maximize sensitivity

[3] This assumes linear elasticity and therefore the quasi-static operating range (bandwidth) is delimited by the first resonant mode.

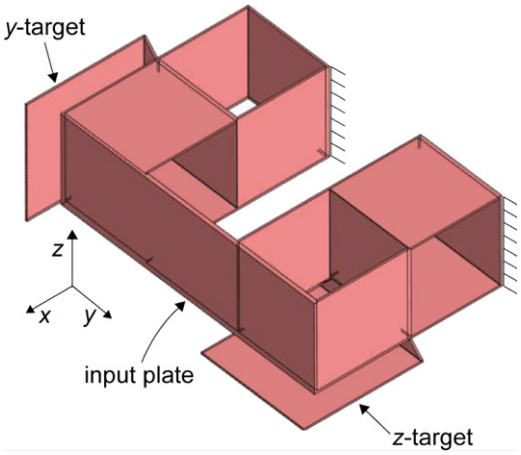

Figure 1. Concept drawing of the two-axis sensor. The sensor consists of four parallel dual cantilever modules arranged in a novel series–parallel configuration. A load in the plane of the input plate can be measured by decoupled, orthogonal motions of the target plates.

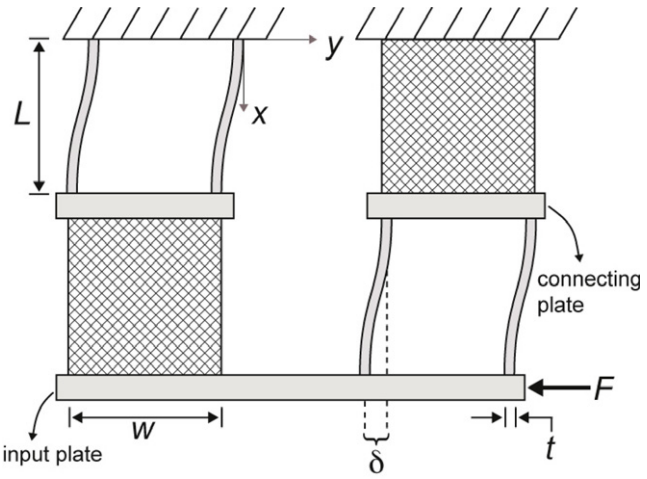

Figure 2. Compound beam structure projected to the x–y plane. Not shown are the displacement targets.

and bandwidth (the product of the two can be thought of as the *sensor quality*) for characterization of microrobots and manufactured using a simple meso-scale manufacturing paradigm. Figure 1 shows the notional design for this force sensor.

Another metric of interest is the sensor resolution. For a given sensitivity, the sensor resolution can be maximized by minimizing the noise. There can be three sources of noise for such a system: electrical, mechanical, and thermal. Electrical noise is minimized by the choice of the sensor which measures the resulting displacement along with accompanying signal conditioning. To minimize mechanical complexity we are using non-contact displacement sensors to measure the displacement of the target plates. Non-contact displacement sensors can be capacitive, inductive, or optical (figure 10 shows the completed sensor with two capacitive sensors measuring the target deflections). All electrical connections are shielded and ground loops avoided to reduce electrical noise. Mechanical noise (vibrations) are minimized by placing all components of the sensor on a vibration isolation table in a room with no air flow. Thermal noise can arise from temperature fluctuations which would then induce a thermal expansion in the sensor materials, leading to erroneous measurements. The sensor structure is constructed from the metal alloy FeNi36 (Invar), which has one of the lowest coefficients of thermal expansion of any known metal alloy [16].

This paper will first describe analytical and numerical models of the static and dynamic performance of the configuration shown in figure 1 in section 2. We will then move on to describe the fabrication and assembly process in section 3. Section 4 will compare the empirical results with the analytical and numerical predictions as well as present a demonstration of the sensor operation by measuring the forces generated by a flapping-wing microrobot. Finally, section 5 discusses these results in the context of the state of the art in force measurement.

2. Sensor modeling and design

The static and dynamic properties of the mechanical structure are determined with analytical models and numerical simulations. The analytical models use simple beam theory and energy equivalence methods. The resulting model for static and dynamic performance is then used to determine an optimal geometric design. The chosen design is then verified numerically using static and eigenfrequency simulations in Comsol and Matlab.

2.1. Analysis of a two-axis compound cantilever

The concept in figure 1 contains four dual (parallel) cantilever modules (two for each sensing axis). Each of the two branches contains a series combination of two dual cantilever modules oriented orthogonally to each other. The dual cantilever modules are assumed to be compliant in the sensing direction and rigid in both normal directions. For example, figure 2 shows the notional design from figure 1 projected onto the x–y plane with a load on the input plate in the $-y$ direction. In this case the upper-left and bottom-right dual cantilever modules are deflected and the upper-right and bottom-left modules are undeformed. Since the two deformed dual cantilever modules are identical, and because of the off-axis rigidity of the other two dual cantilever modules, the two deformed dual cantilever modules are in parallel. Because of this, and because of the symmetric nature of this design (with respect to loads in the y and z principle directions), the analysis consists of (a) bending analysis for a single dual cantilever module and (b) parallel combinations of the modules.

First, the relationship between the beam deflection and the moment distribution is given by simple beam theory:

$$\frac{\partial^2 y}{\partial x^2} = \frac{M(x)}{EI} \tag{1}$$

where the moment distribution for a clamped-guided beam is $M(x) = F(L/2 - x)$. It is important to note, for modeling and questions of mechanical failure, that we are assuming

linear elasticity and small strains. Integrating this twice and considering boundary conditions yields the displacement for any point on the beam:

$$y(x) = \frac{F}{EI}\left(\frac{L}{4}x^2 - \frac{1}{6}x^3\right). \tag{2}$$

At the distal end of the beam ($x = L$), the free end displacement is:

$$y(L) \equiv \delta = \frac{FL^3}{12EI} \tag{3}$$

where δ is the distal lateral displacement as defined in figure 2. From this we can derive the stiffness of a single clamped-guided cantilever beam. The concept shown in figure 1 shows modules of dual cantilevers mounted in an orthogonal series–parallel configuration. The stiffness of one dual cantilever module is equal to two clamped-guided beams in parallel, and the complete compound structure in figure 2 is equivalent to two parallel clamped-guided beams in parallel. Therefore, the relation between a load at the input plate and the deflection of the target plate is the total stiffness given by the following:

$$k_{\text{tot}} = \frac{48EI}{L^3} = \frac{4Et^3w}{L^3} \tag{4}$$

where t, w, and L are the thickness, width, and length of an individual clamped-guided beam respectively (defined in figure 2). The sensitivity of the force sensor is simply the displacement sensor sensitivity (in V m^{-1}) divided by this stiffness. Of course, the stiffer the beam, the less sensitive the force sensor.

To determine the bandwidth of the sensor, we calculate the natural frequency of the beam. For this, we use an energy method to relate the kinetic energy of the compound beam to that of an idealized system.

$$\tfrac{1}{2}m_{\text{eq}}\dot{\delta}^2 = \tfrac{1}{2}\int \rho\dot{y}(x)^2\,\mathrm{d}V = \tfrac{1}{2}\rho A\int_0^L \dot{y}(x)^2\,\mathrm{d}x \tag{5}$$

where $y(x)$ is given in equation (2). Combining equations (2) and (3) and reordering to give $y(x)$ as a function of the free end displacement results in the following:

$$y(x) = \delta\left[\frac{3x^2}{L^2} - \frac{2x^3}{L^3}\right]. \tag{6}$$

Equation (6) can now be used in the energy equivalence of equation (5):

$$\frac{1}{2}m_{\text{eq}}\dot{\delta}^2 = \frac{1}{2}\rho A\dot{\delta}^2\int_0^L\left[\frac{3x^2}{L^2} - \frac{2x^3}{L^3}\right]^2\mathrm{d}x. \tag{7}$$

Solving this gives the equivalent mass of a single parallel beam structure as a function of mass of the beam elements: $m_{\text{eq}} = m_{\text{b}}\frac{26}{35}$, where m_{b} is the combined mass of the two parallel plates that make up the parallel cantilever module ($= 2\rho \times$ length $\times$ width $\times$ thickness). For either sensing axis, the structure in figure 1 is composed of two dual cantilever modules in parallel, so the effective mass of connected dual cantilever modules must be doubled. Furthermore, there are other components which will add to the kinetic energy including the connecting plate between orthogonal dual cantilever modules (only one for each sensing axis, see figure 2), the input plate, the target plate, and the assumed mass of the load (i.e. the device connected to the input plate).

Table 1. Invar parameters used for analytical and numerical simulations.

Parameter	Units	Value
Density, ρ	(kg m^{-3})	8100
Modulus, E	(GPa)	141
Loss factor, η	—	0.0007
Poisson's ratio, ν	—	0.29
Coef. thermal expan., α	(10^{-6} K^{-1})	1.2

$$\begin{aligned} m_{\text{tot}} &= 2\left(m_{\text{b}}\frac{26}{35}\right) + m_{\text{b}} + m_{\text{conn.}} + m_{\text{input plate}} + m_{\text{target}} + m_{\text{load}} \\ &= m_{\text{b}}\frac{87}{35} + m_{\text{conn.}} + m_{\text{input plate}} + m_{\text{target}} + m_{\text{load}}. \end{aligned} \tag{8}$$

Some of the additional mass terms are intrinsic functions of the cantilever geometries, as will be discussed below. Finally, since both sensing axes have identical mass and stiffness properties, it is sufficient to estimate the first mode of a single axis. This is simply given as follows:

$$f_1 = \frac{1}{2\pi}\sqrt{\frac{k_{\text{tot}}}{m_{\text{tot}}}}. \tag{9}$$

Note that we are assuming linear elasticity and this is the first resonant mode. The (quasi-static) bandwidth of the sensor will be slightly less than this so that the resonant modes are not present in measurements (the measurements will be filtered with a low-pass filter of a cut-off frequency sufficiently below this value). Since this analysis assumes linear dynamics, it is simple to derive not only the resonant frequency, but the frequency response by writing the equation of motion for the sensor as follows:

$$m_{\text{tot}}\ddot{\delta} + k_{\text{tot}}(1 + \mathrm{i}\eta)\delta = F_0\mathrm{e}^{\mathrm{i}\omega t}. \tag{10}$$

The damping term is included as the loss factor, η. The material parameters of Invar are given in table 1. This completes the analytical model of the sensor; given equations (4), (8)–(10), all the relevant sensor characteristics can be derived.

Earlier, the sensor quality was defined as the product of sensitivity and bandwidth (not dissimilar to the gain-bandwidth product of operational amplifiers).

$$Q' \equiv f_1 \times 1/k_{\text{tot}} \propto \sqrt{\frac{1}{k_{\text{tot}}m_{\text{tot}}}}. \tag{11}$$

Maximizing the sensor quality as a function of the material and geometric properties will result in an optimal configuration, however the search can be narrowed further given specific sensing requirements. Since the dimensionality of this optimization problem is low, a simple brute-force search method is used to span a reasonable space of the geometric parameters. The constraints on the search are the desired

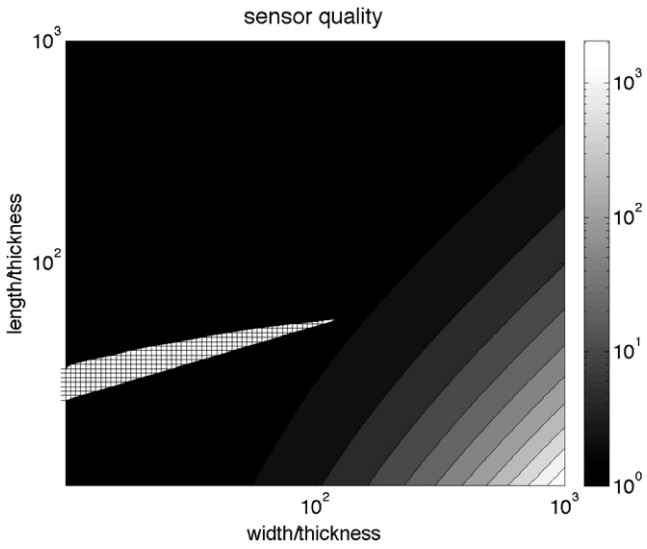

Figure 3. Results from a brute-force optimization on the sensor quality. The hatched area encompasses points in the geometry space that meet the requirements for the target microrobotics application.

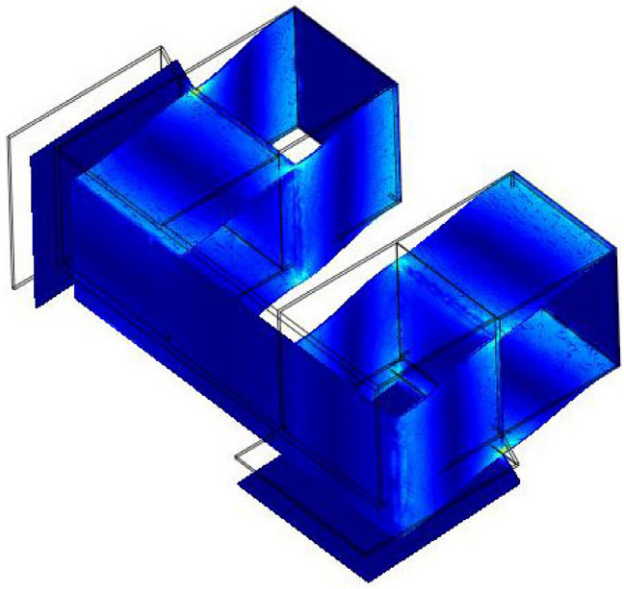

Figure 4. Results of the numerical analysis show negligible coupling between the two axes. The load is applied tangentially to the distal face and the central plates move in orthogonal directions.

Table 2. Results of geometric optimization using constraints from the target application. Note that the mass of the connector and input plates are a function of the width and thickness. The mass of the target plate is a function of the capacitive sensor head size and the material thickness; the target must have sufficient area to cover the capacitive sensor head.

Parameter	Units	Value
Width, w	(mm)	7
Length, L	(mm)	7
Thickness, t	(μm)	150
Load mass, m_{load}	(mg)	200
Conn. mass, $m_{\text{conn.}}$	(mg)	60
Target mass, m_{target}	(mg)	108
Input plate mass, $m_{\text{input plate}}$	(mg)	186

sensitivity and bandwidth. The target application is the characterization of lift and drag forces for a flapping-wing robotic insect. For this application the desired sensitivity and bandwidth are derived from the body mass and wingbeat frequency of the fly respectively. For a fly mass of approximately 100 mg, flapping at 100 Hz [14], we can set the requirements of 1% body mass force resolution with a bandwidth of 10× the fundamental (wingbeat) frequency. Therefore, the load mass, m_{load}, is estimated to be 200 mg (to account for the body mass, as well as a conservative estimate for the mass of the connection between the fly and the input plate). With these minimum constraints (10 μN resolution and 1 kHz bandwidth) and the 200 mg load mass, the model described above can be used to choose geometric optimality for the unknown parameters of the sensor. The sensor quality is shown as a function of the sensor geometry in figure 3. Those values which satisfy the design criterion are represented by the hatched area. The chosen geometry is summarized in table 2.

2.2. Numerical analysis

Given the results of the optimization from the previous discussion, a physical model is created to match the geometry and material properties. This is imported into Comsol for static and dynamic analysis. For static analysis, a load (equivalent to the robotic fly's body mass) is applied tangentially to the input plate, and the displacements of the target plates are measured to calculate the stiffness. This is also used to verify that the motions of the target plates are solely in the desired directions. An example of the resulting deformation (exaggerated) is shown in figure 4.

Similarly, the frequency response is determined by applying a harmonic force to the input plate and measuring the target displacement across a range of excitation frequencies. This is compared to the solution to equation (10) in figure 5. Note that the results show similar first resonant peaks but the numerical simulation shows higher modes that would not be predicted with the linear simulation.

3. Fabrication

The entire sensor is fabricated from a single flat sheet by a process of laser micro-machining and folding. The 3D design in figure 1 is mapped onto a 2D surface consisting of cut lines and perforated (fold) lines. These cut and fold lines are then micro-machined using a Q-switched, pulsed Nd:YVO_4 (355 nm), galvanometer-steered laser operating at 20 kHz. Once cut, the input plate is reinforced with laminated layers of high strength, low weight S2-glass weave reinforced epoxy composite. Once folded, tabs are soldered together to complete the structure. The sensor is shown flat in figure 6(a) and folded in figure 6(b).

Finally, the sensor is mounted to a PCB such that the y and z axes correspond to the global horizontal and vertical

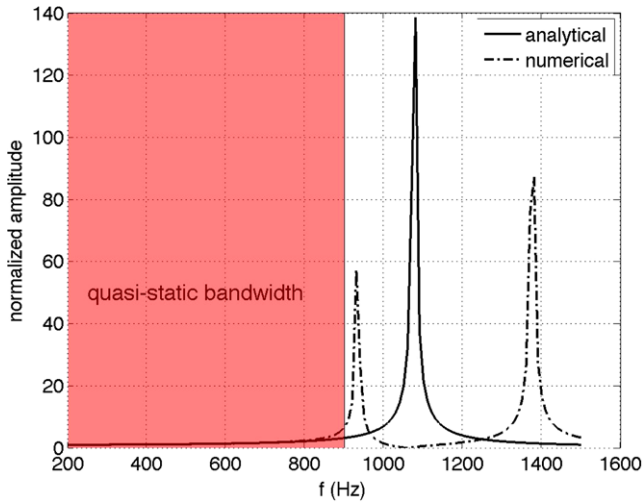

Figure 5. Frequency response as predicted from numerical and analytical simulations. The parameters are derived from the geometry in table 2 and material properties in table 1.

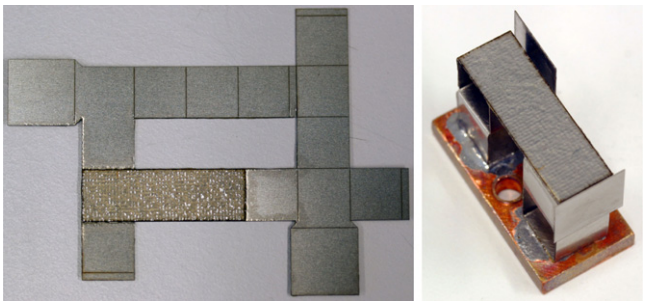

Figure 6. The sensor is constructed from the low-CTE alloy Invar. 2D sheets of Invar are laser-micro-machined to create cut lines and perforated lines (a). Once cut, the Invar sheet is folded into the 3D structure shown (b).

directions respectively. Two capacitive sensors, each mounted to a 5DOF manipulator to enable precise positioning of the displacement sensors with respect to the force sensor, are positioned appropriately. Semiconductor strain-gauges were also considered for displacement transduction. These gauges typically have gauge factors between 50 and 200 [17], compared to 2–5 of metal foil strain-gauges. However, semiconductor strain-gauges suffer from high sensitivity to temperature and will drift continuously, especially in environments with high intensity illumination for high speed videography (as with our applications). The displacement sensors are from Physik Instrumente, model D-510.020 capacitive sensor with the E-852 single channel signal conditioners (0.2 nm resolution, sensitivity $= 1$ V μm^{-1}, 20 μm sensing range, and 6.6 kHz bandwidth). Figure 7 describes this setup and how an applied load alters the measured capacitance. Since the alignment of the sensor heads to the displacement targets is crucial, a vision camera is included to assist with positioning the capacitive sensor head in the required proximity of the target plates. Once the sensor heads are aligned, the frequency response of the sensor is determined with application of an impulse, as shown in figure 8.

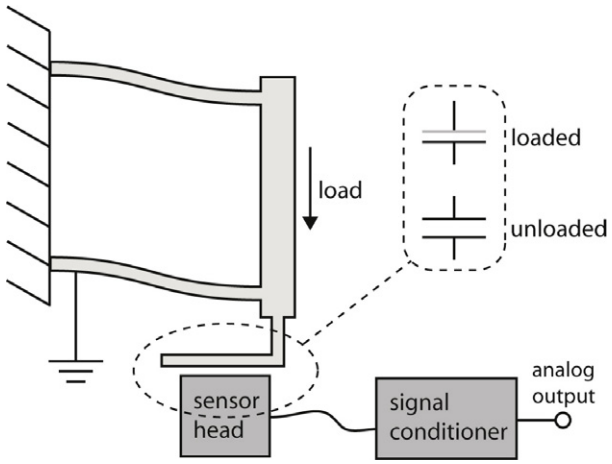

Figure 7. Schematic of the capacitive displacement sensor. Under load, the gap between the target plate and the sensor head changes, altering the capacitance between the two surfaces.

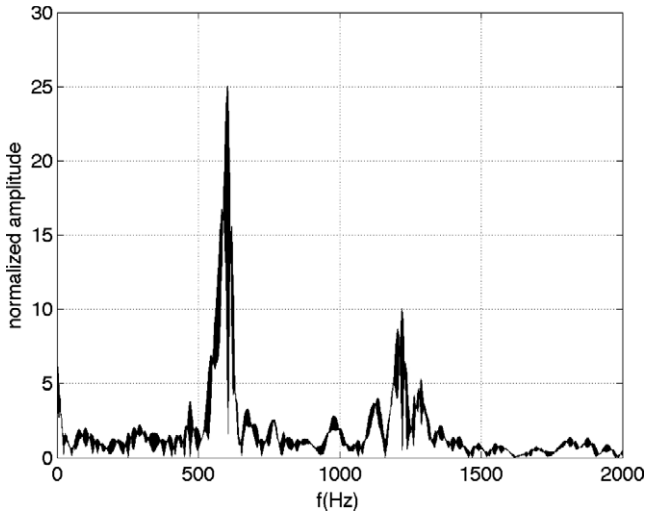

Figure 8. Frequency response (in the z-axis).

Calibration is accomplished using pre-measured discrete weights as opposed to known forces or displacements [5]. Due to the complexity of the alignment mechanisms, it is not possible to rotate the force sensor to calibrate the horizontal sensing axis. Instead, a custom low friction pulley was created using spring-loaded jewel bearings. This is shown in figure 9 along with the resulting calibration curves. Note the linearity of the response.

4. Results

The results of the analytical, numerical, and experimental studies are summarized in table 3. The analytical and numerical predictions are very well correlated. Empirical results show higher sensitivity and smaller bandwidth than expected. The larger sensitivity can be explained by a $\sim 1/3$ reduction in the stiffness compared to the predicted value. The lower bandwidth is consistent with the reduced beam stiffness coupled with a 70% increase in the expected load mass. The

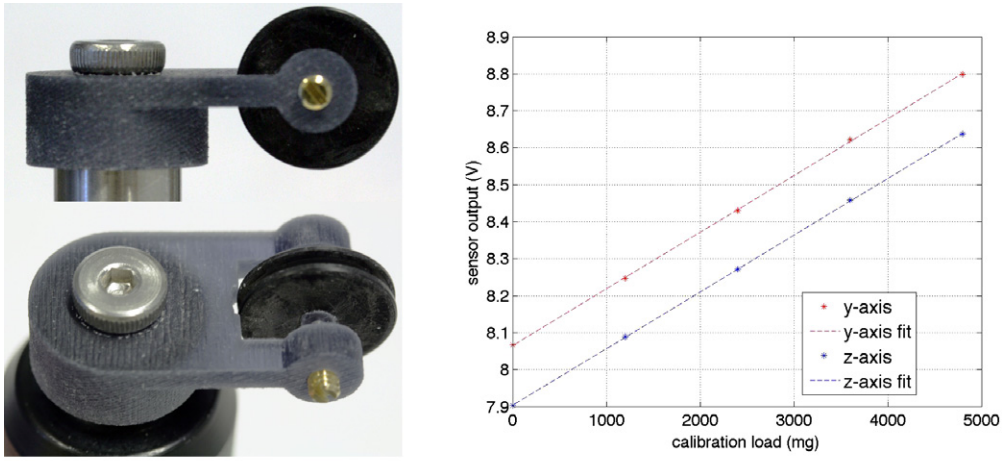

Figure 9. Calibration pulley for the horizontal axis (a) and calibration curves for both axes (b).

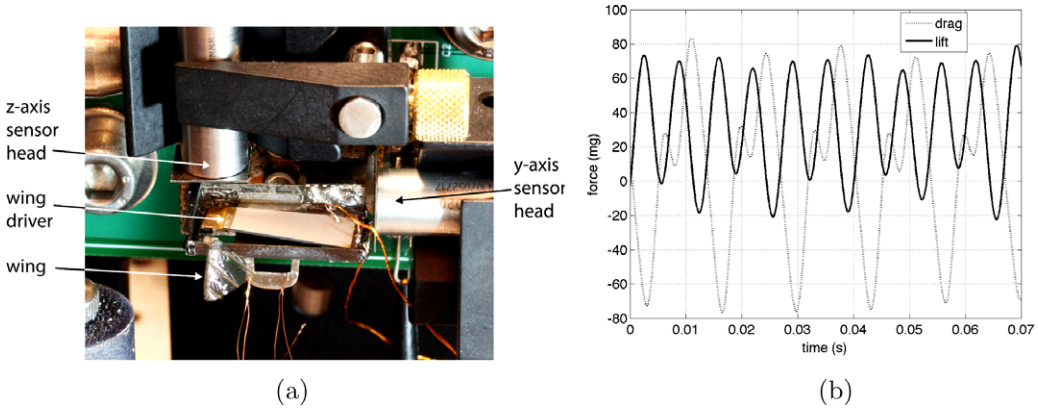

Figure 10. The sensor with a microrobotic fly connected to the input plate (a). The sensor is used to measure the lift and drag forces generated by the flapping wings (b). This is the first time-resolved measurement of lift and drag forces from an insect-scale robot.

Table 3. Analytical, numerical, and experimental characteristics of the force sensor. Bandwidth calculations are based upon an expected 200 mg load mass. Resolution predictions are based upon the analytical and numerically derived compliances and the 0.2 nm quoted displacement sensor resolution. Range is determined by the beam compliances and the quoted sensor range.

	Analytical	Numerical	Experimental
k_{tot} (kN m^{-1})	38.8	37.5	25.6
Sensitivity (V N^{-1})	25.77	26.67	39.07
Resolution (μN)	7.76	7.5	5.12
Bandwidth (Hz)	1076	930	630
Range (N, p–p)	0.78	0.75	0.51

extra load mass can likely be attributed to the thermoplastic adhesive that is used to fix the device under test to the input plate. This highlights a practical challenge for effective use of high performance load cells: the device under test must be securely fixed to the sensor, however this attachment should require minimal additional structural elements or adhesives.

Finally, our robotic insect is fixed to the input plate using a temporary adhesive. The flies wings are driven open-loop, obtaining a pre-determined wing trajectory (similar to that of natural insects). The forces tangential to the input plate are measured: by the convention in figure 10, the lift is the y-axis force and the drag is obtained by a homogeneous transformation applied to the z-axis force (to account for the rotation of the wing). The resulting forces are shown in figure 10. This is the first time-resolved measurement of the lift and drag forces from a fly-sized microrobot.

5. Discussion

We have demonstrated the design, analysis, and fabrication of a novel force sensor which attempts to address the conflicting requirements of bandwidth and sensitivity for many force sensing applications. There are several advantages to this design. First, it is modular; the notional geometry in figure 1 can be redesigned with a different geometry to achieve a different force/displacement relationship. This is independent of the displacement sensor since the displacement sensor is non-contact. Second, the sensor itself is very robust to handling during manufacturing. Finally, the sensor is simple to rapid prototype and can easily be mass-produced.

Possible applications for this technology include robotic manipulation for precise assembly, characterization of biological processes, precision manufacturing, and inexpensive multi-axis scales. Our primary application, as shown in figure 10, is the characterization of flapping-wing aerodynamics for a robotic insect. This tool will now enable us to correlate the forces generated by flapping-wing devices at the scale of their insect counterparts with the wing trajectories and the airfoil design. We feel this is an essential tool for the development of more in-depth models for the mechanics and aeromechanics of such devices. Furthermore, this application illustrates the need for a high sensor quality due to the demanding sensitivity and bandwidth requirements.

References

[1] Kim D-H, Sun Y, Lee S and Kim B 2005 Investigating chorion softening of zebrafish embryos with a microrobotic force sensing system *J. Biomech.* **38** 1359–63

[2] Shen Y, Wejinya U, Xi N and Pomeroy C 2007 Force measurement and mechanical characterization of living drosophila embryos for human medical study *Proc. Inst. Mech. Eng.* H **221** 99–112

[3] Autumn K and Peattie A 2002 Mechanisms of adhesion in geckos *Integr. Comp. Biol.* **42** 1081–90

[4] Nafari A, Karlen D, Rusu C, Svensson K, Olin H and Enoksson P 2008 MEMS sensors for *in situ* TEM atomic force microscopy *J. Microelectromech. Syst.* **17** 328–33

[5] Cui Y, Dong W, Liu M, Wang M, Wang J, Wang X and Wang L 2007 Preliminary study of calibration system for PZT thin film micro force sensor *Ferroelectrics* **358** 22–8

[6] Saeidpourazar R and Jalili N 2008 Microcantilever-based force tracking with applications to high-resolution imaging and nanomanipulation *IEEE Trans. Indust. Electron.* **55** 3935–43

[7] Wood R J and Fearing R S 2001 Flight force measurements for a micromechanical flying insect *IEEE/RSJ Int. Conf. on Intelligent Robots and Systems (Maui, HI)*

[8] Dao D, Toriyama T, Wells J and Sugiyama S 2003 Silicon piezoresistive six-degree of freedom force-moment micro sensor *Sensors Mater.* **15** 113–35

[9] Beckwith T G and J H Lienhard V 1993 *Measurement of Force and Torque* 5th edn (Englewood Cliffs, NJ: Prentice-Hall) pp 537–70

[10] Minne S, Manalis S and Quate C 1995 Parallel atomic force microscopy using cantilevers with integrated piezoresistive sensors and integrated piezoelectric actuators *Appl. Phys. Lett.* **67** 3918

[11] Sun Y, Fry S, Potasek D, Bell D and Nelson B 2005 Characterizing fruit fly flight behavior using a microforce sensor with a new comb-drive configuration *J. Microelectromech. Syst.* **14** 4–11

[12] Beyeler F, Muntwyler S, Nagy Z, Graetzel C, Moser M and Nelson B 2008 Design and calibration of a MEMS sensor for measuring the force and torque acting on a magnetic microrobot *J. Micromech. Microeng.* **18** 025004

[13] Tibrewala A, Phataralaoha A and Buttgenbach S 2008 Simulation, fabrication and characterization of a 3D piezoresistive force sensor *Sensors Actuators* A **147** 430–5

[14] Wood R J 2008 The first flight of a biologically-inspired at-scale robotic insect *IEEE Trans. Robot.* **24** 341–7

[15] Lu Z, Chen C and Lin W 2006 Force sensing and control in micromanipulation *IEEE Trans. Syst. Man. Cybern.* C **36** 713–24

[16] Woolger C 1996 *Mater. World* **4** 332–3

[17] Window A L 1992 *Semiconductor Strain Gauges* (London: Elsevier Applied Science) pp 267–89